

NGAO trade study report: LGS asterism geometry and size KAON 429 (WBS 3.1.2.3.3)

Ralf Flicker (*rflicker@keck.hawaii.edu*)

W.M. Keck Observatory, 65-1120 Mamalahoa Hwy., Kamuela, HI 96743, USA

14 November 2006

Abstract

This report addresses the LGS tomography wavefront error as a function of asterism type and size. The goal is to assess how many LGSs are required to meet the performance criteria, as outlined in the June 2006 NGAO proposal, and to find the simplest asterism that enables a critical mass of the science cases listed there. It is found that the 5-LGS configuration that has been at the focus of studies so far (the “quincunx”) falls short on most accounts. Alternative asterisms with 7-9 LGSs are investigated and found to offer significantly improved all-around performance over the quincunx. In conclusion, a candidate asterism consisting of 8 LGS (with a “bimodal” layout) is identified and proposed as a new baseline NGAO configuration for future studies.

1 Introduction

From the NGAO WBS dictionary definition of task 3.1.2.3.3, “LGS Asterism Geometry and Size”:

Find the simplest LGS asterism geometry meeting the performance budget goals (e.g. quincunx, ring, 1+triangle, or hex) and the asterism radii. Consider optimization of the Strehl of the tip/tilt stars and the resultant sky coverage as well. Complete when LGS asterism, HO WFS, and LO WFS requirements have been documented.

While this trade study goes through a number of different investigations related to the tomography error and its scaling laws, what is being pursued overall is on the one hand an evaluation of the current default asterism (i.e. the quincunx, 5a, cf. Fig. 3). The question is whether this asterism can deliver the required performance in all science cases. Secondly, the goal is also to quantify the performance of a number of alternative asterisms and make a direct comparison to the quincunx. In the course of going through these various investigations, this trade study supplies:

- + Some refinement to the wavefront error budget “LGS tomography error”
- + A basis for iterating on the wavefront error budget
- + Support for other related trade studies (e.g. NGS, sky coverage)
- + A recommendation for potential LGS solutions for Keck NGAO

A few things that this trade study does *not* do include:

- Calculating what the resulting sky coverage will be, as this depends upon the particular science case and the NGS system architecture adopted, which is the target of a different trade study
- Issuing a definitive verdict on which LGS asterism should be chosen, since this decision must be based on the complete performance budgets for each science case, and not a single term (i.e. the tomography error) of the wavefront error budget

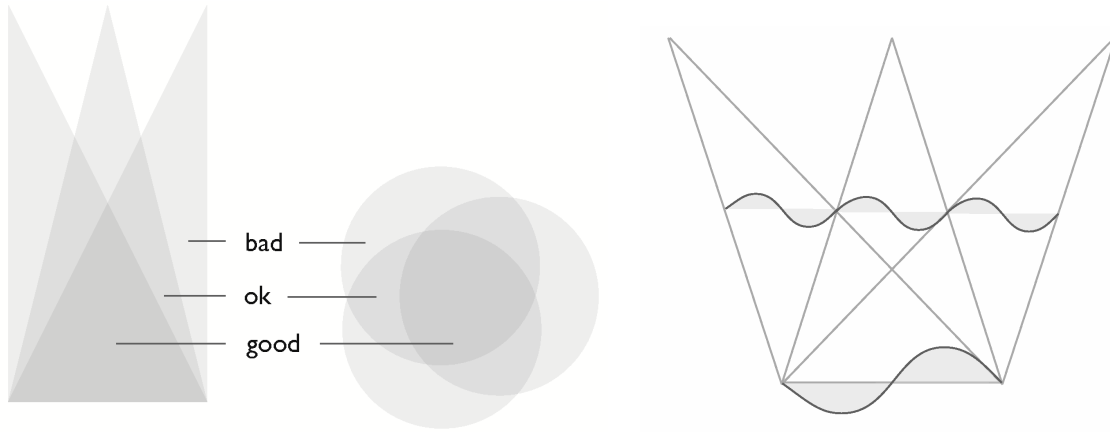


Figure 1: Cartoon illustrating the issue of sampling (left) and invisible modes (right) in multi-beacon LGS AO systems. Atmospheric tomography, i.e. the three-dimensional measurement of turbulence-induced wavefront aberrations, is only deterministic for the patches where two or more beacons overlap. Invisible modes (and null-modes) are a class of three-dimensional modes that cancel out in the direction of each LGS and result in a zero measurement, but the modes do not cancel out for NGS and not in between the LGS.

1.1 Tomography errors

What is investigated and reported on in this trade study is a single term of the wavefront error budget, which in the 18 June 2006 NGAO proposal was labeled “LGS Tomography error”[2]. This term can be broken down into a collection of contributing factors, which potentially could all be analyzed separately. The approach taken in the current study, however, is to follow the structure of the existing wavefront error budget and report the error in a single term referred to as the tomography error. The terminology adopted in this text may be at variance with that of other authors. There is unfortunately no “Blue Book of MCAO” laying down the canon of tomography speak, so different words are sometimes used to describe the same phenomenon. By offering a comprehensive description of the usage of the terms in this document, however, there should be no confusion. The individual terms that contribute to the overall tomography error are listed below:

Sampling. This type of error results from two circumstances: turbulence that is not sampled at all, and turbulence that is sampled with insufficient tomographic information. It is clear that the former constitutes an uncorrectable error since the aberration is never measured. For the second category, the three-dimensional determination of turbulence-induced wavefront aberrations requires that the aberrations are sampled by at least two beacons from different angles, by a principle similar to triangulation or parallax measurements. Patches of the volume turbulence that are only sampled by one beacon can not be solved for its vertical distribution deterministically, and the best that can be done in reconstruction with that information is to distribute it vertically according to statistical a priori assumptions.

Invisible modes. Some part of the modal content of atmospheric turbulence falls into a category called invisible modes, signifying that they are registered as zero measurements by all the WFSs, but in between the WFS beacons they are non-zero and contribute to the wavefront error seen by a science instrument. In the case of LGS beacons, these modes also become non-zero for beams focused at infinity in the direction of the LGSs. These modes are by necessity three-dimensional, and are rendered invisible to the AO system by a conspiracy in which modes at different altitudes cancel out within the beam print to leave only piston in each beam, which is not sensed.

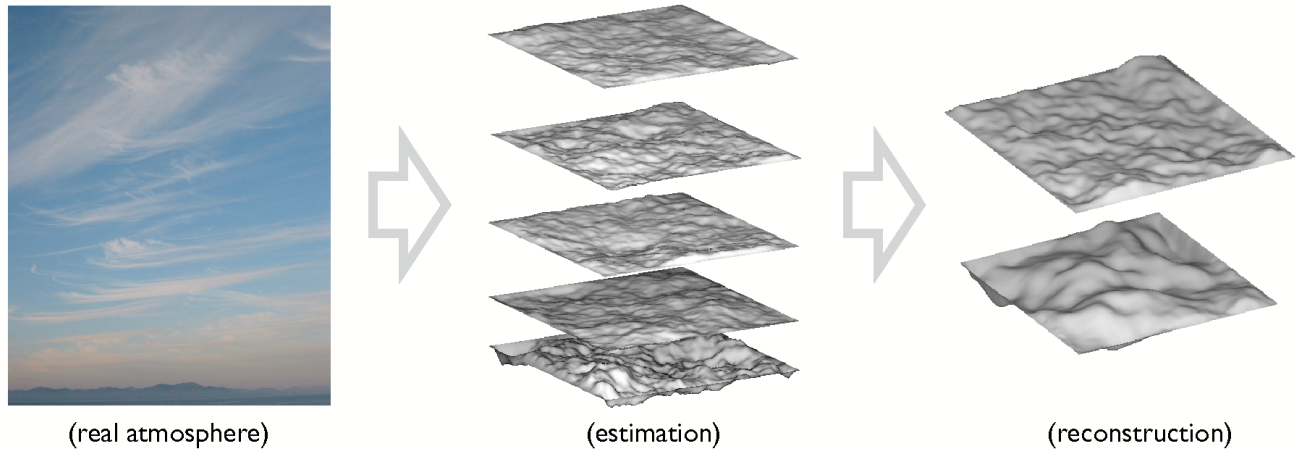


Figure 2: Cartoon illustrating the estimation and reconstruction steps of the tomographic wavefront reconstruction process.

Null-modes. A special case of invisible modes are the so-called null-modes, which are particular to a LGS-based tomography system (as opposed to NGS-based). The null-modes arise from combinations of modes that only cancel out partially and leave, in addition to piston, also linear (i.e. tip/tilt) terms in the beam. When these terms are filtered in a LGS system, due to the tilt determination problem with LGSs, the result is a loss of information that renders the system blind to these modes as well. These differential tilt modes (sometimes called “plate-scale modes” because of their effect, or “null-modes” because they belong to the null space of the LGS interaction matrix) are produced by a combination of quadratic modes (e.g. focus, astigmatism) occurring at different altitudes. Hence, in the Kolmogorov model of atmospheric turbulence, these modes have relatively large weights in the turbulence power spectrum, and the impact of not correcting them can be severe (see e.g. Ref. [5]).

Estimation. The estimation step takes all the available WFS data and produces an estimated three-dimensional refractive index profile. Apart from sampling errors that are propagated right through, this estimation in itself comes with an intrinsic error that is governed chiefly by the algorithm employed and the accuracy of a priori turbulence statistics invoked therein. Typically, this algorithm applies a layered model where the vertical turbulence distribution is mapped onto a small number of layers approximately representative of the real atmosphere. Apart from the horizontal resolution, which is an algorithm parameter, each layer has two free parameters that must be adjusted to produce the best fit to the real atmosphere: its conjugation altitude, and its statistical weight. But even under the most fortuitous of circumstances, it is clear that some error must result from the instance of fitting a continuous quantity to a sparsely layered model.

Reconstruction. The final step of the tomography process is to fit the above estimated turbulence profile to the physical wavefront correction elements in the system, e.g. the DMs. Since it is likely that the number of DMs, their conjugation altitudes and their spatial resolutions are all going to be different from the estimator model of the preceding paragraph, another fitting procedure must be carried out to complete the wavefront reconstruction process. This algorithm is typically a least-squares projection, and a certain amount of control is possible in this step in how the wavefront errors are distributed over the field of view. Hence the final reconstruction error is very dependent upon the mechanisms of this algorithm, as well as the quantity and distribution of spatial wavefront correction devices available for implementing the three-dimensional wavefront correction.

1.1.1 Minimum variance estimator

In the open-loop minimum variance estimator (MVE), the two steps of estimation and reconstruction (also referred to as “fitting”) are represented algebraically by the mappings

$$E_* : s \mapsto x \in \mathcal{R}^{N_{\text{est}}}, \quad (1)$$

$$F_* : x \mapsto a \in \mathcal{R}^{N_{\text{act}}}, \quad (2)$$

where the starting point $s \in \mathcal{R}^{N_{\text{mes}}}$ is the vector of WFS measurements, x is the estimated refractive index profile, and a is the vector of DM actuator commands. In their simplest form the estimation and fitting matrices can be written (cf. e.g. Ref. [7])

$$E_* = [G_x^T C_n^{-1} G_x + C_x^{-1}]^{-1} G_x^T C_n^{-1}, \quad (3)$$

$$F_* = [H_a^T W H_a]^{-1} H_a^T W H_x. \quad (4)$$

In the estimator E_* , $G_x : x \mapsto s$ is the influence matrix from refractive index to WFS measurements, C_n is the WFS noise covariance matrix and C_x is the refractive index covariance matrix. In the reconstructor F_* , $H_a : a \mapsto w$ is the mapping from actuator commands to wavefronts w , $H_x : x \mapsto w$ is the mapping from refractive index profile x to wavefronts w , and W is a weighting matrix that specifies how to prioritize the final wavefront error over the field of view. Both of these matrices represent least-squares solutions, in the above formulation resulting in a minimization of the phase variance, consequently maximizing the Strehl ratio (hence why this type of solution is sometimes also referred to as a Strehl optimal estimator).

1.2 LTAO, SCAO, MCAO and MOAO

These more or less standardized acronyms require little introduction, but for completeness their usage in the current text are defined here. While single-conjugate AO and laser tomography AO are sometimes used interchangeably, the former (SCAO) does not tell you whether it is a multi-beacon WFS system, but you know that there is only one DM. The latter (LTAO) implies the use of multiple LGSs, but does not specify how the correction is applied. However, if LTAO was used in conjunction with multiple DMs, we would call it MCAO. Hence, we take the definition of LTAO to be a multi-LGS single-DM tomography system, and consequently SCAO is a single-DM single-beacon “conventional” AO system.¹ If a LTAO system is used in conjunction with one or several additional open-loop controlled narrow-field DMs (dedicated to a single “object”), we will call it multi-object AO (MOAO).

1.2.1 MCAO vs. MOAO

From a wavefront reconstruction perspective, both MCAO and MOAO relies on a multi-beacon tomography system producing an estimate of the volume turbulence as a first step. In other words, they share a common estimation matrix E_* as exemplified in (3), and up to this point the MCAO and MOAO wavefront reconstruction processes are identical. Loop issues aside, they differ only in they formulation of the fitting matrix F_* as exemplified in (4). In the case of MCAO, F_* is constructed to optimize the performance over a given field of view, by weighing together line integrals of the back-projected wavefronts (last step of Fig. 2) through the specified field optimization points. In the MOAO case, this projection can be visualized as a two-step process: the ground-layer is reconstructed exactly as in the MCAO case (this part of the F_* matrix can thus also be identical). The wavefront to put on the open-loop MOAO unit is also computed quite similarly to the MCAO case, with the difference that a single field point has been encoded into the remaining matrix structure with a weight of one, hence optimizing performance for that specific direction.

¹Some combinations were left out, but seeing as multi-NGS tomography systems are currently out of fashion there should be no confusion.

TURBULENCE PROFILE

h_l (km)	0	0.5	1	2	4	8	16
c_l	0.67	0.05	0.062	0.051	0.078	0.051	0.045

INTEGRATED PARAMETERS

seeing	r_0	θ_0	d_0	\bar{h}
0.65''	0.156 m	3.10''	5.60 m	3.26 km

Table 1: Summary of equivalent mean model atmosphere for Mauna Kea.

In principle, MOAO and MCAO need not be mutually exclusive; one could run an MCAO system with additional open-loop MOAO units operating in parallel (for instance, operating outside of the field of view of the altitude-conjugated DMs, for e.g. sharpening of low-order NGS). If the altitude-conjugated DM in a MCAO system and the open-loop DM in a MOAO system have identical resolutions and are defined on a common grid, the MOAO DM shape can even be exactly a subset of the MCAO upper DM shape. Hence the close similarity between the two modes of operation, and also their expected performance with regards to the tomography error.

1.3 Trade study specifications

1.3.1 Mauna Kea turbulence model

The parameters of the equivalent mean model atmosphere are summarized in table 1, and the quantities are defined as follows:

$$r_0^{-5/3} = 0.423k^2 \sec(\zeta) \mu_0, \quad (5)$$

$$\theta_0^{-5/3} = 2.914k^2 \sec^{8/3}(\zeta) \mu_{5/3}, \quad (6)$$

$$d_0^{-5/3}(H) = k^2 \left[0.5 \mu_{5/3}^-(H) H^{-5/3} - 0.452 \mu_2^-(H) H^{-2} \right], \quad (7)$$

$$\bar{h} = \left(\frac{\mu_{5/3}}{\mu_0} \right)^{3/5}, \quad (8)$$

$$\mu_m^-(H) = \int_0^H dh h^m C_n^2(h), \quad (9)$$

$$c_l = \int dh g_l(h) C_n^2(h), \quad (10)$$

where $k = 2\pi/\lambda$ is the wave number, H is the LGS altitude ($H = 90$ km), ζ is the zenith angle and $\sec(\zeta)$ is the air mass. The Fried parameter r_0 quantifies the spatial coherence of the turbulence and is directly related to the overall seeing. The isoplanatic angle is a measure of the angular coherence of the turbulence, and \bar{h} is an equivalent turbulence height. These quantities are related by $r_0 \propto \bar{h} \theta_0$. The nameless parameter d_0 is used to quantify the focal anisoplanatism associated with a LGS beacon at height H . It can be thought of as the parameter that allows the focal anisoplanatism phase variance to be written $\sigma_{\text{FA}}^2 = (D/d_0)^{5/3}$, where D is the diameter of the telescope aperture.

The turbulence model of table 1 was constructed from two sources. The basis for choosing the median seeing level was a collection of seeing statistics recorded between 2000-2004 by three Mauna Kea telescopes as presented in Ref. [1]. This led to a median r_0 value of 15.6 cm at zero zenith angle. The free atmosphere turbulence profile (i.e. coefficients c_1 to c_6) was based on MASS data from the TMT monitoring site called 13-North, from December 2005 to October 2006 (see Ref. [4]). Combining the two data sets, the ground-layer strength (i.e. the coefficient c_0) could be deduced, and the full turbulence profile constructed as shown above.

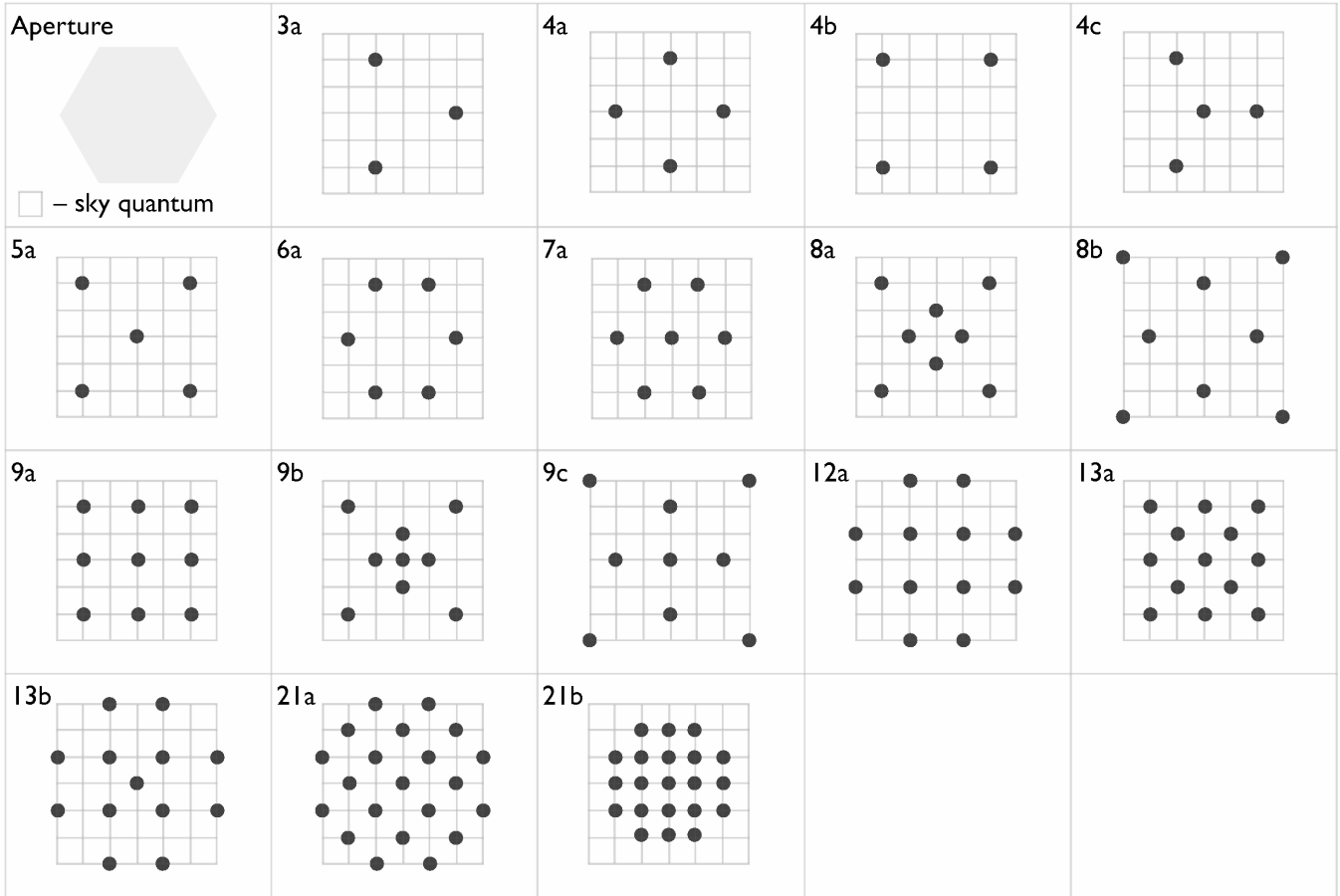


Figure 3: LGS asterisms included in this study. The rectangular grid visualizes the sky quantization imposed by the simulation tool, resulting in a coarse grid that restricts the shape of the possible asterisms. The dot patterns are not all drawn to the same scale in this figure; the underlying grid may be stretched or compressed isotropically to a limited degree, changing the apparent size of the asterisms without altering their relative geometry.

1.3.2 NGAO system model

This study adopts the baseline NGAO dimensions from the June 2006 NGAO proposal:

- **WFS:** The wavefront sensors are all linear slope sensors of the Shack-Hartmann type with 48 sub-apertures across the telescope pupil, resulting in a sub-aperture size of approximately 21 cm. The slope measurement is perfectly linear, noise-free and aliasing-free, and have no centroiding errors associated with it.
- **LGS:** The LGS configuration is varied between the asterisms shown in Fig. 3. Spot elongation, LGS position uncertainty, sodium layer structure and fluctuations are all omitted from the modeling.
- **Telescope:** The telescope pupil is modeled as a binary transmission function with a monolithic hexagonal shape, without segment gaps or the saw-tooth outline produced the hexagonal segment shapes.
- **Control:** An all-open-loop system with zero delay is simulated.
- **DM:** The DM resolutions are matched to the WFS in a Fried type geometry. By the nature of the simulation (cf. Appendix A), the high-spatial-frequency DM fitting error is zero. The DM configuration is varied only between two modes:

1. Only one DM conjugated to zero altitude (LTAO mode).
2. For MCAO and MOAO, a second DM is added at a non-zero conjugation altitude. In the case of MOAO, the second DM becomes a place holder in the simulation, and the shapes of the open-loop MOAO DMs are computed as subsets of this (oversized) DM (cf. Appendix A for more details on the MOAO implementation).

The idealized component modeling outlined above may sound much too idealized for representing a real AO system, which it certainly is. The point however is that by this mode of modeling, whereby most of the traditional AO errors are not included in the scope of the simulation, the *only* errors being measured are LGS tomography errors; i.e. sampling, invisible modes, estimation and reconstruction. This is a good thing, since it is much harder to extract the tomography error from an all-in simulation that includes a host of other AO errors related to WFS and DM imperfections, limited bandwidth, etc. This is in line with the underlying assumption of the NGAO wavefront error budget draft, that these AO error terms are uncorrelated and can be measured independently.

1.3.3 Simulation

Several aspects of the simulation have been touched upon already, and here are only mentioned the remaining main assumptions and specifications that are directly relevant to the trade study. For more details on the simulation tool, the reader is referred to Appendix A and Refs. [3], [6].

Quasi-static loop. Although it was stated above in relation to the control system that there was no delay in the loop, for practical reasons, zero delay is impossible to simulate in this tool. By setting the wind speeds of the turbulence layers to a small value and keeping the WFS integration times and other loop delays at their nominal values, a quasi-static scenario was effectuated. Although this does not result in zero bandwidth error, the error was measured to be very small. The combined effect of quasi-static temporal modeling and the fundamental limits of the MAP estimator were measured to be between 1-2 nm RMS (as deduced from running a NGS case which has no tomography error). This was deemed small enough when considered in quadrature with the tomography error as to be safely ignored in this trade study.

Turbulence averaging. Obtaining results that are representative of the statistics are one important aspect of Monte Carlo simulations. The quasi-static scenario described in the previous paragraph would seem to result in very poor averaging. The way this simulation handles averaging over turbulence statistics in a quasi-static scenario is by a combination of “skip-ahead” and going through a number of completely independent sets of phase screens. Skip-ahead means jumping ahead in time by a large number of frames (~ 500) within the current set of phase screens, and resume averaging over a different part of that set. With seven layers all moving in different directions and at different speeds, one can skip around like this for quite a while before running out of unique statistics. But to complement this method, after a certain number of skips, the phase screens themselves were replaced by a new, completely independent set. After each skip or new set of screens, 5 frames were allowed for convergence before performance evaluation resumed.

Performance evaluation. Through this study, when quoting the measured tomography error it is the tilt-removed error that is reported. Although the simulation includes a NGS-based null-mode compensation system, some residual differential tilt may remain even under idealized noise-free conditions. This reflects the fundamental limitations of a null-mode system that measures and corrects a limited number of modes (only five modes in this case). Hence, by removing uncorrected tip and tilt when computing the wavefront error over the field of view, we avoid counting residual null-mode errors to the high-order tomography wavefront error budget. Null-mode errors are to be addressed in a separate trade study.

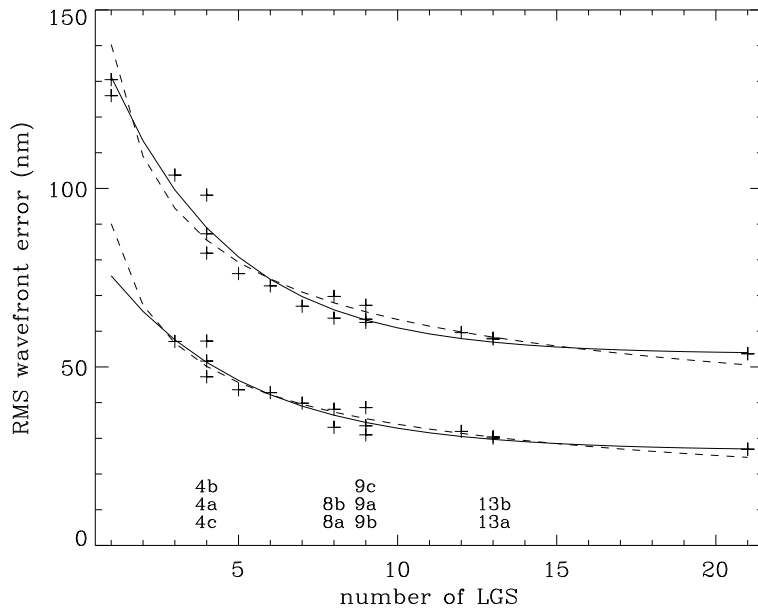


Figure 4: Tomography wavefront error versus number of LGS, for the asterisms in Fig. 3. The asterism sizes were adjusted to optimize the on-axis performance at zenith. Solid line is the fit to the data obtained by an exponential function, and the dashed line is the fit obtained assuming a $-5/12$ power law, as suggested by NGS theory. The two families of curves represent the conservative (upper) and ideal (lower) tomography assumptions.

Tomography assumptions. The actual performance of a tomographic reconstruction algorithm in a real scenario depends on a number of design choices in constructing the algorithms, and how sensitive they are to discrepancies between the model assumptions that went into the algorithms and the reality of the atmosphere at the time of observation. It is the opinion of the author that these uncertainties should be addressed at some level, and the range of possible performance levels due to tomography accuracy explored. The approach taken in this study is to follow through two extreme but opposite cases of tomography assumptions for every parameter study that is undertaken. These two scenarios are designed to provide what may be considered to be bounding curves for the worst case performance (henceforth referred to as the “conservative” case) and the best case scenario (henceforth referred to as the “ideal” case). While both of these extremes are possible but not very likely performance levels, one would be justified in making design choices based upon an interpolation that lies between these two extremes. The middle region between these two bounding curves represents an average condition that is neither too optimistic nor too pessimistic, with room for both improvement and deterioration. See Appendix A for details on how these two cases were realized in the simulation tool.

2 Parameter studies

2.1 Number of LGS in asterism (LTAO)

The tomography error versus asterism geometry (although plotted as a function of the number of beacons) is shown in Fig. 4, for the asterisms listed in Fig. 3. The asterisms were all optimized for on-axis LTAO performance, resulting in LGS radii corresponding to column 1 of table 2. A simple exponential function of the form

$$f(x) = a_0 + a_1 \exp(a_2 x) \quad (11)$$

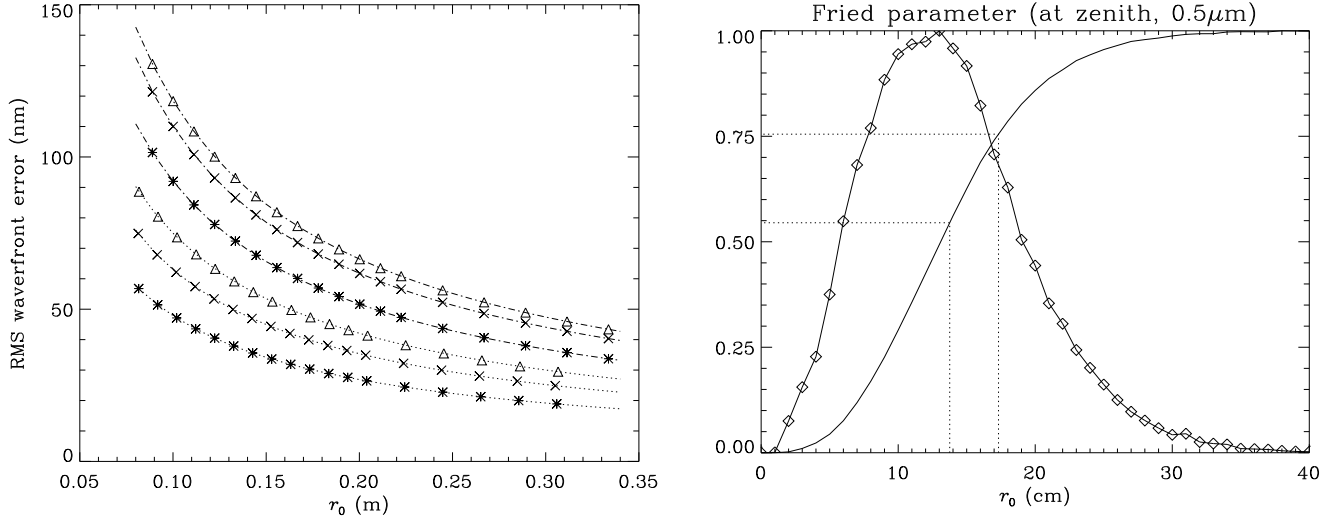


Figure 5: Left: tomography wavefront error versus r_0 (at zenith) for the asterisms 4c (triangles), 5a (X) and 8a (asterisks). Dotted lines are curve-fits to a two-parameter power law, very closely matching the theoretically predicted $-5/6$ power law. The two families of curves represent the conservative (upper) and ideal (lower) tomography assumptions. Right: typical histogram and cumulative distribution function of r_0 .

produces a good fit to the data, as indicated by the solid line curves in Fig. 4. Also plotted (dashed line curves) is the fit produced by a power-law with a fixed exponent of the form

$$f(x) = a_0 + a_1 x^{-5/12}. \quad (12)$$

In the case of NGS asterisms with a simple ring-like geometry, it was shown (see Ref. [8]) that the tomography error may be expressed as

$$\sigma_{\text{tom}}^2 = \langle \epsilon_{\text{tom}}^2 \rangle \propto \left(\frac{\Theta}{\gamma_K} \right)^{5/3}, \quad (13)$$

where γ_K is called the tomographic patch size and Θ is the angular radius of the asterism. For the sake of comparison, we may relate Θ to the average density of beacons and obtain the approximate proportionality $\Theta \propto N^{-1/2}$, where N is the number of beacons. Substituting into 13 results in the approximate power law $\sigma_{\text{tom}} \propto N^{-5/12}$.

The main points to take away from this graph is: 1) that there is a point of diminishing returns beyond which adding more LGS does very little to improve on-axis performance, and 2) that there is a significant difference between the conservative and ideal tomography cases. The latter will be a recurring statement throughout this study.

2.2 Seeing, r_0 (LTAO)

While this trade study does not explicitly call for an evaluation of tomography performance versus seeing conditions, it is nevertheless instructive to look at it in some capacity. Figure 5 (graph on the left) shows the tomography error versus r_0 (at zenith) for three different asterisms (4c - triangles, 5a - X, 8a - asterisks), again optimized for on-axis performance in LTAO mode. The dotted lines over-plotted are curve-fits based on the power-law function

$$f(x) = a_0 x^{a_1}. \quad (14)$$

From the same NGS theory that produced equation (13) we have that $\gamma_K \propto r_0$, which substituted into (13) directly gives the prediction $\sigma_{\text{tom}} \propto r_0^{-5/6}$. From the six individual curve-fits computed we obtain a mean value of the exponent $a_1 = -0.83326 \pm 0.00018$, to be compared with the predicted value $-5/6 = -0.83333\dots$. This is a rather

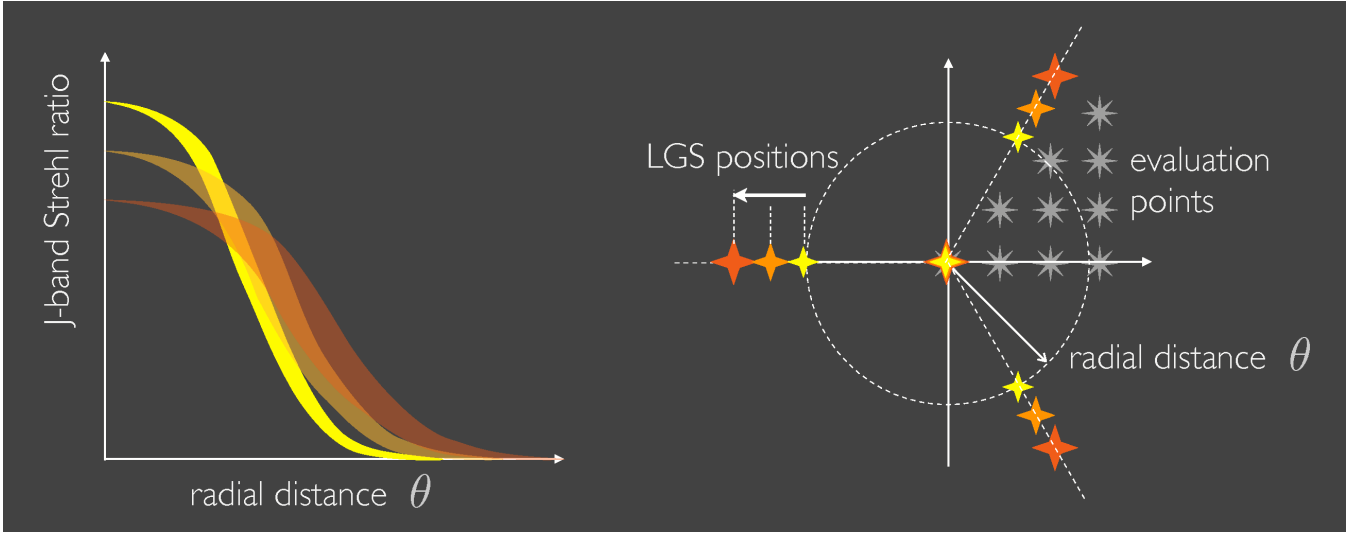


Figure 6: Cartoon illustrating the variables of the wide-field plots in Figs. 8-11.

remarkably accurate reproduction of analytical theory by a Monte Carlo simulation. Of pointed interest in Fig. 5 is the substantial improvement over all seeing conditions that is bought by going from 5 to 8 LGS in the asterism. From this perspective, we can see that a denser asterism (e.g. 8a) will be able to meet a given performance requirement a larger fraction of the time. Naturally, this is an anticipated result, but combining the information in the left-hand plot of Fig 5 with a plot of the cumulative distribution function (CDF) of r_0 as shown on the right, we can get a more quantitative estimation of the effect. Note that this is *not* the CDF of the Mauna Kea summit ridge, but only an illustrative sample. As an example, let's pick the benchmark performance 70 nm RMS as a fictitious science goal, and estimate our science efficiency assuming the conservative tomography scenario. Reading from the plot, asterism 8a crosses 70 nm at $r_0 = 13.8$ cm, and asterism 5a at $r_0 = 17.3$ cm. Carrying those two numbers over to the CDF plot, we find the corresponding percentiles to be 0.545 and 0.755. In other words, by going from asterism 5a to 8a, in this (fictitious) example we increase the efficiency of this science target from 24.5% to 45.5%, or in relative terms almost a doubling.

2.3 Asterism size (MOAO/MCAO)

While all parameter studies up to this point have focused on and been optimized for on-axis performance, this last section of the parameter studies investigates the performance over a larger field of view as a function of asterism size, for a subset of different asterisms. Because the resulting plots contain a lot of information and make use of color coding, a graphic in Fig. 6 illustrates the layout and the variables of the following figures 8-11. Each panel corresponds to a given asterism, and displays the RMS wavefront error (left) and J band (1250 nm) Strehl ratio (right) as functions of the radial distance from the central axis. Within each panel, the family of different-colored curves correspond to different asterism sizes, as quantified by the approximative radius of the asterism outline given in table 2. In addition, the survey is done both for the conservative and ideal tomography assumptions, the results of the former appearing in Figs. 8 and 9, and the ideal cases in Figs. 10 and 11.

Covering a range of LGS densities between 4-13 stars in the asterism, these plots fill in some of the gaps left by the preceding on-axis performance estimates by showing how the performance over a wide field of view is governed by the asterism size and LGS density. We also see the pronounced difference between asterisms that have the same number of beacons, but differ in their arrangement to have either uniform or non-uniform LGS densities (e.g. comparing asterisms 9a and 9b). By having an enhanced density of LGS around the center, asterism 9b retains a higher performance around the central region of the field of view as the constellation is enlarged, without for that

Asterism	LGS positions				
	1	2	3	4	5
4c	7.0	14.0	21.0	28.0	35.0
5a	7.9	15.9	23.8	31.8	39.7
7a	7.2	14.4	21.6	28.8	35.9
9a	7.3	14.6	21.8	29.1	36.4
9b	8.5	17.1	25.6	34.1	42.6
13a	7.3	14.6	21.8	29.1	36.4

Table 2: Approximate asterism radii in arc seconds, for the curves plotted in Figures 8-12. The radii were calculated as the average radial distance of the outer “ring” of beacons. Colors ranging from black to yellow in the figures span the LGS positions 1-5 respectively in the above table.

reason taking any significant penalty in the outer parts of the field. Comparing asterisms 9a and 9b, it may look like 9a, with its uniformly square arrangement of beacons, has a more even performance level within the LGS field of view, but this is chiefly due to the 9b performance being so much better than 9a in the central region rather than it being so much worse in the wide field. Apart from investigations like these, that trade the benefits of one particular asterism/size over some other combination, one of the principal uses of these plots may be in estimating the degree of sharpening of null-mode NGS operating in the J band, as provided by the LGS tomography system out to a radial field of view of 100 arc seconds. This information may be used by other trade studies that look to the optimization of the null-mode NGS system with regards to AO performance and sky coverage.

3 Science cases

In the June 2006 NGAO proposal a number of representative science cases were modeled for the wavefront error budgets presented in Section 14 of the Appendix [2]. The science cases relevant to LGS tomography were: KBOs, Galactic Center, Field Galaxies, GOODS-N, and a “Best case NFAO”. The error budgets prepared for these science scenarios were all based on the quincunx asterism (5a), and an estimation of the LGS tomography error calculated in each case. The parameters and assumptions of these cases relevant to the LGS tomography errors are summarized in table 3.

Some minor differences between the assumptions of the proposal wavefront error budgets and the new simulations should be pointed out. The 10'' LGS radius quoted for the science cases using the LTAO mode were not carried over directly into the new simulations. Instead, the previously derived asterism sizes that optimized the on-axis LTAO performance were used in the new simulations. Also, these optimal asterism radii had originally been obtained for zero zenith angle, and were not re-optimized here for the various zenith angles of the proposal science cases, but were only scale geometrically to retain the same relative proportion to a collimated beam as in the zero zenith angle case. Checking the validity of this assumption revealed a negligibly small deviation from the optimal asterism size (~ 1 nm RMS). The Mauna Kea equivalent mean model atmosphere used throughout this trade study was employed also for the replication of the science cases, with only the r_0 adjusted to match that of the NGAO proposal.

The results of the new simulations are presented in the right-hand part of table 3. In addition to the quincunx (5a), asterism 8a was simulated for comparison. The two columns of RMS wavefront errors (in nm) give the estimated tomography error in both the conservative/ideal tomography scenario, and the final column specifies the radius of the point in the field of view where the performance was measured. For the MOAO science cases, the full details of the performance evaluation are given in Ref. [3]. From these numbers, it is clear that the quincunx will have problems meeting the science requirements even in the most optimistic tomography scenario. In general, there are only a few available options to deal with shortcomings revealed by this science case point comparison:

Science case	from NGAO proposal					new simulations		
	AO mode	LGS radius	zenith angle	$r_0(0)$	σ_{tom} (nm)	5a	8a	eval.
KBO	LTAO	10''	48°	0.18	29	89/59	69/36	0''
Galactic Center	LTAO	10''	48°	0.18	29	89/59	69/36	0''
Best case NFAO	LTAO	10''	5°	0.40	29	38/25	29/15	0''
Field galaxies	MOAO	21''	30°	0.18	118	175/105	160/75	25''
GOODS-N	MOAO	33''	45°	0.18	160	280/170	240/100	30''

Table 3: Sample science cases represented in the NGAO proposal wavefront error budgets.

- Change asterism, invoke more LGS at the expense of system complexity and cost. Cost is presumably the main throttle here, and as was shown in Section 2.1, the LTAO cases quickly enter a region of diminishing returns after ~ 9 LGS.
- Change assumptions by e.g. requiring better seeing conditions, at the expense of reduced science efficiency. This relates to the study in Section 2.2 which showed how one can buy science efficiency by adding LGS, and conversely, save dollars but cut back on the science efficiency by reducing the number of LGS.
- Adopt a more optimistic tomography assumption and move closer to the “ideal” scenario, by assuming that our on-sky wavefront reconstruction abilities will be better than the average condition simulated in this trade study. This may prove to be a valid strategy, but currently there is little data to support it, and until there is more reliable data, a slightly more conservative approach may be advisable.
- Find ways to lower other terms of the wavefront error budget. This may become a necessary countermeasure if the current science case requirements on the LGS tomography wavefront error are found to be too costly to realistically accommodate by adding more LGS.

4 Conclusions

Based on the science case point comparisons of the preceding section, it seems clear that the quincunx asterism (5a) will be unable to deliver the required LGS tomography performance in all cases, under the given seeing conditions. Barring relaxed requirements from the science cases or a substantial improvement of the average seeing on Mauna Kea, the NGAO system will most likely need to look to alternative asterism that can deliver higher performance levels. Taking into account the points made in sections 2.1, 2.2 and 2.3, as well as the realism of having a finite budget for building the instrument, it seems like a reasonable recommendation that future studies and iterations on the NGAO performance budgets should look at asterisms having in the range of 7-9 LGS. The final choice should be deferred until much more comprehensive simulations have been conducted using a tool like e.g. LAOS [7], but as a starting point, this trade study nominates the three asterisms in Fig. 7 (i.e. asterisms 7a, 8a and 9c) for the

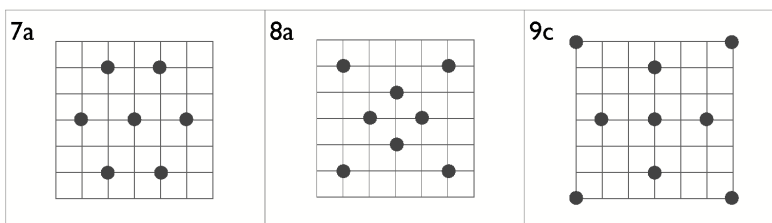


Figure 7: Recommended asterisms for further NGAO studies.

final round of the asterism grand prix. Out of the three, 8a is currently the personal favorite of the author, as being a relatively modest investment above 5 LGS but offering substantially improved all-around performance and flexibility compared to the quincunx.

Some exciting possibilities open up with asterisms like 8a and 9c, whose bimodal structure consist of a “core” LGS cluster with a “ring” of perimeter LGS. One can imagine having the core and the ring WFS clusters grouped into two classes mounted on separate optical stages that allow the two groups to be scaled in size independently of each other, adjusting the resulting LGS density between settings optimized for wide field performance and MOAO, to settings that emphasize the on-axis performance and LTAO, to anything in between. That would certainly make life interesting for the one who has to see to it that the wavefront reconstruction algorithms are always up to date. One may also think of Rayleigh rejection strategies that launch the core LGS cluster from behind the secondary mirror, and the perimeter LGS from the side of the primary mirror, in order to minimize the fratricide effect.

A Simulation tool

A.1 Simulation approach

Coming up at some point, for now check out Ref. [6].

A.2 Code validation

See Fig. 13.

References

- [1] Gemini Ground Layer Adaptive Optics Fesibility Study Report. 23 February 2005.
- [2] The Next Generation Adaptive Optics System at the W. M. Keck Observatory. A proposal for design and development (v. 19), June 18, 2006.
- [3] R. Flicker. NGAO system design phase trade study report: LGS asterism geometry and size. Presentation given at the 2nd NGAO team meeting at Caltech, 14 Nov 2006.
- [4] R. Flicker. Mauna Kea turbulence statistics from the TMT MASS/DIMM and weather station at the 13-North site. Technical Report KAON 415, W.M. Keck Observatory, 22 September 2006. KAON 415.
- [5] R. Flicker and F. Rigaut. Tilt anisoplanatism and PSF retrieval in LGS MCAO using a predictive controller. In E. Vernet, R. Ragazzoni, S. Esposito, and N. Hubin, editors, *Beyond conventional adaptive optics : a conference devoted to the development of adaptive optics for extremely large telescopes. Proceedings of the Topical Meeting held May 7-10, 2001, Venice, Italy. Edited by E. Vernet, R. Ragazzoni, S. Esposito, and N. Hubin. Garching, Germany: European Southern Observatory, 2002 ESO Conference and Workshop Proceedings, Vol. 58, ISBN 3923524617, p. 377, pages 377–+, 2002.*
- [6] R. C. Flicker. Efficient first-order performance estimation for high-order adaptive optics systems. *Astron. Astrophys.*, 405:1177–1189, July 2003.
- [7] L. Gilles and B. Ellerbroek. *LAOS: Linear Adaptive Optics Simulator reference manual*. Thirty Meter Telescope, 2006. LAOS svn revision 76.
- [8] A. Tokovinin and E. Viard. Limiting precision of tomographic phase estimation. *J. Opt. Soc. Am. A*, 18(4):873–882, April 2001.

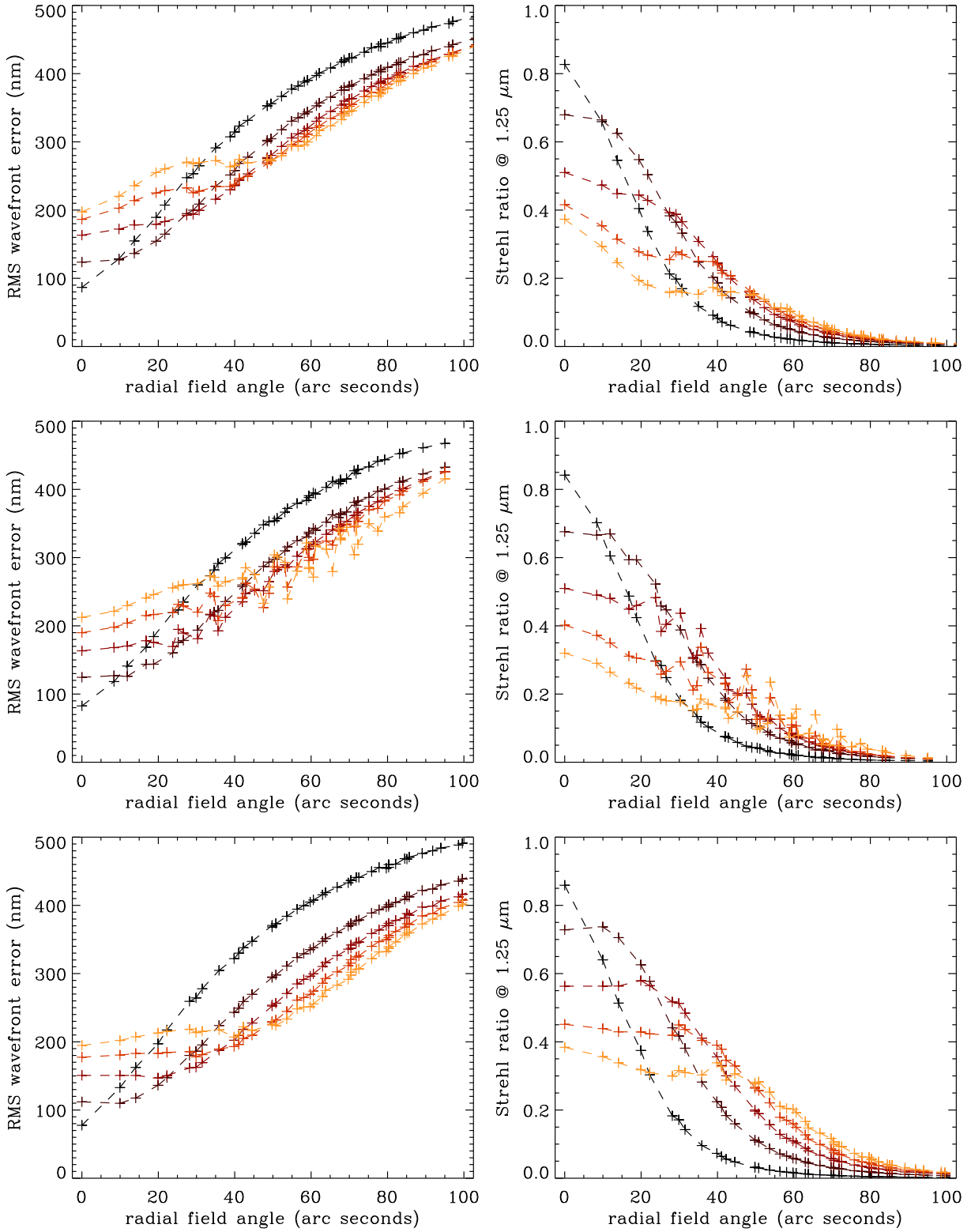


Figure 8: Tomography error over a wide field of view for asterisms 4c (top), 5a (middle) and 7a (bottom) under *conservative* tomography assumptions. Left: RMS wavefront error in nm. Right: J-band Strehl ratio. Colors indicate the asterism sizes varying from on-axis optimized at $\sim 7.5''$ radius (black) to wide-field at $\sim 38''$ radius (yellow). See Table 2 for precise numbers.

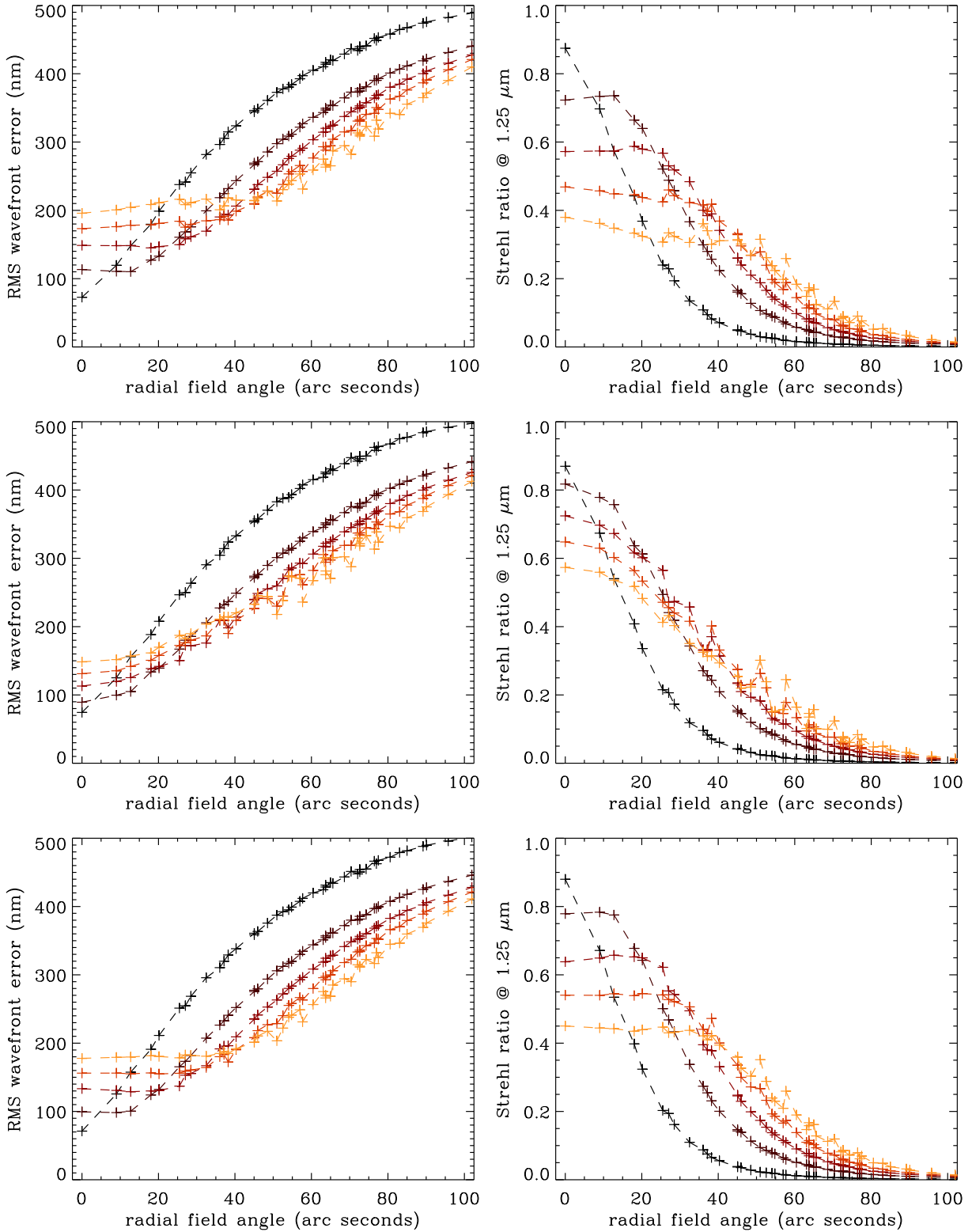


Figure 9: Tomography error over a wide field of view for asterisms 9a (top), 9b (middle) and 13a (bottom) under *conservative* tomography assumptions. Left: RMS wavefront error in nm. Right: J-band Strehl ratio. Colors indicate the asterism sizes varying from on-axis optimized at $\sim 7.5''$ radius (black) to wide-field at $\sim 38''$ radius (yellow). See Table 2 for precise numbers.

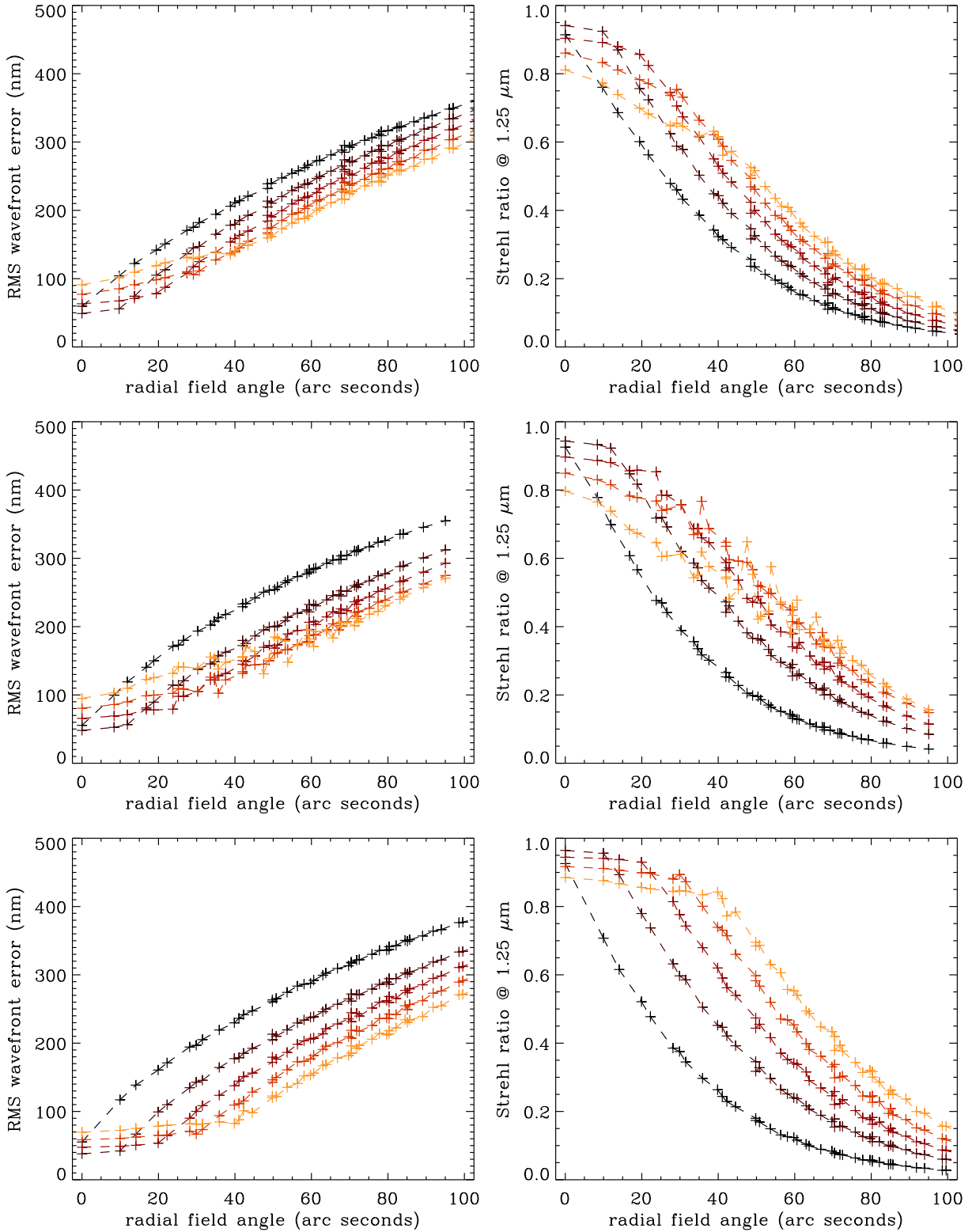


Figure 10: Tomography error over a wide field of view for asterisms 4c (top), 5a (middle) and 7a (bottom) under *ideal* tomography assumptions. Left: RMS wavefront error in nm. Right: J-band Strehl ratio. Colors indicate the asterism sizes varying from on-axis optimized at $\sim 7.5''$ radius (black) to wide-field at $\sim 38''$ radius (yellow). See Table 2 for precise numbers.

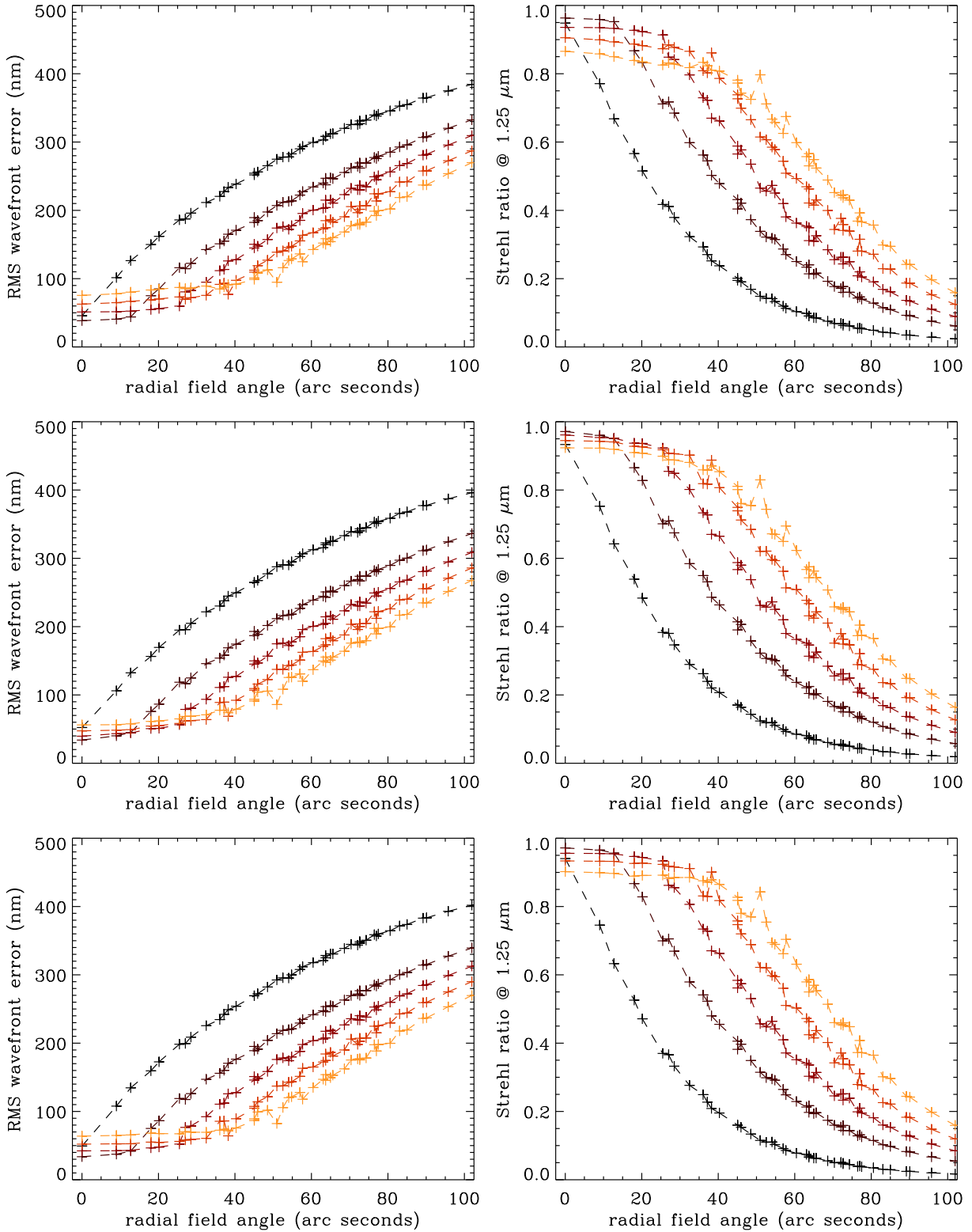


Figure 11: Tomography error over a wide field of view for asterisms 9a (top), 9b (middle) and 13a (bottom) under *ideal* tomography assumptions. Left: RMS wavefront error in nm. Right: J-band Strehl ratio. Colors indicate the asterism sizes varying from on-axis optimized at $\sim 7.5''$ radius (black) to wide-field at $\sim 38''$ radius (yellow). See Table 2 for precise numbers.

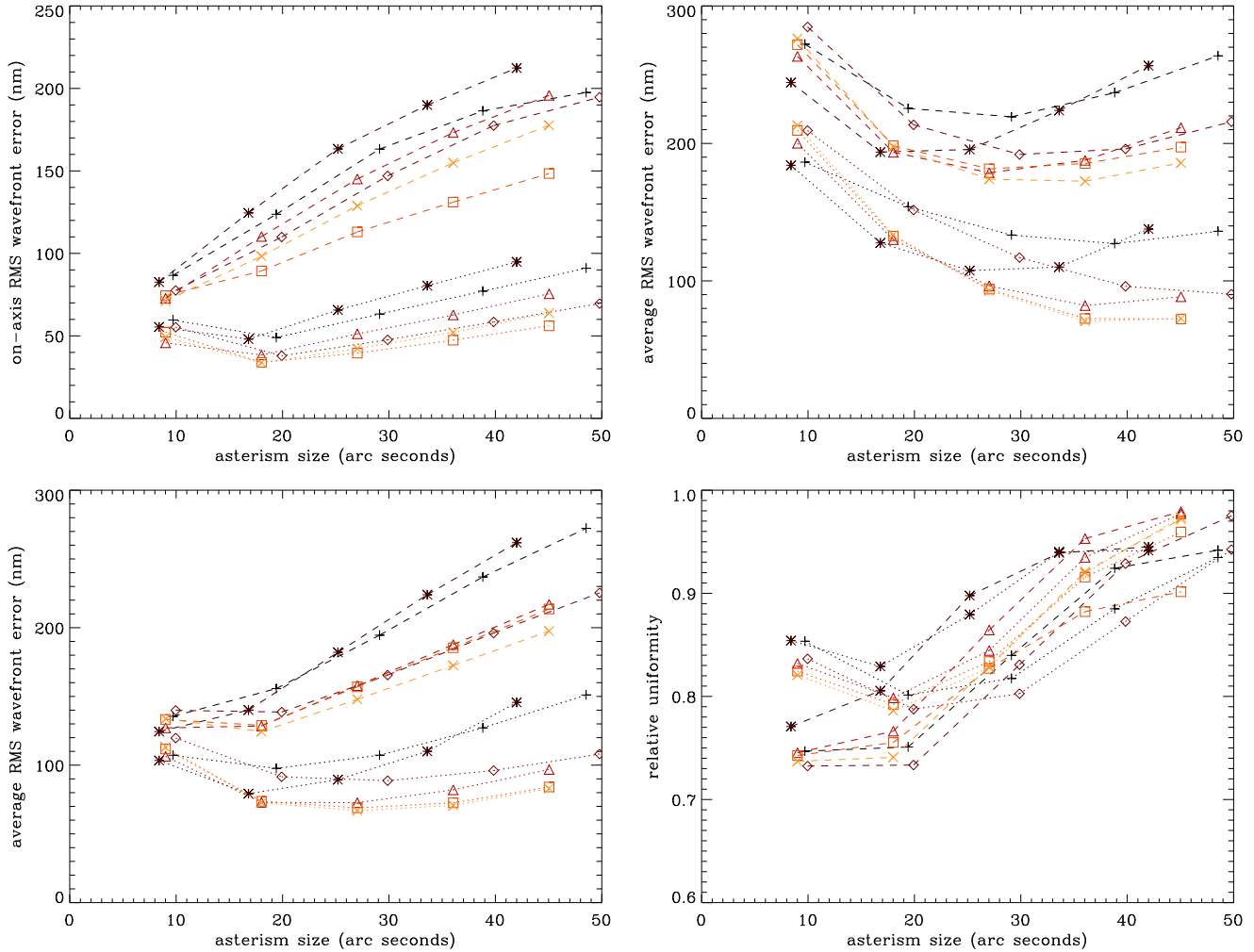


Figure 12: Summary of wide-field tomography error evaluations in Figures 8-11, versus asterism size along the x-axis. The asterisms are identified by: 4c (plus), 5a (asterisk), 7a (diamond), 9a (triangle), 9b (square) and 13a (X). Dashed lines represent conservative tomography assumptions; dotted lines represents the ideal case. Top left: on-axis error. Top right: the average error over 1' field of view. Bottom left: the average error over the field of view spanned by the LGS (i.e. the asterism size). Bottom right: relative uniformity of performance, expressed as $1 - \text{stdev}(\sigma_w) / \text{avg}(\sigma_w)$, over 1' field of view.

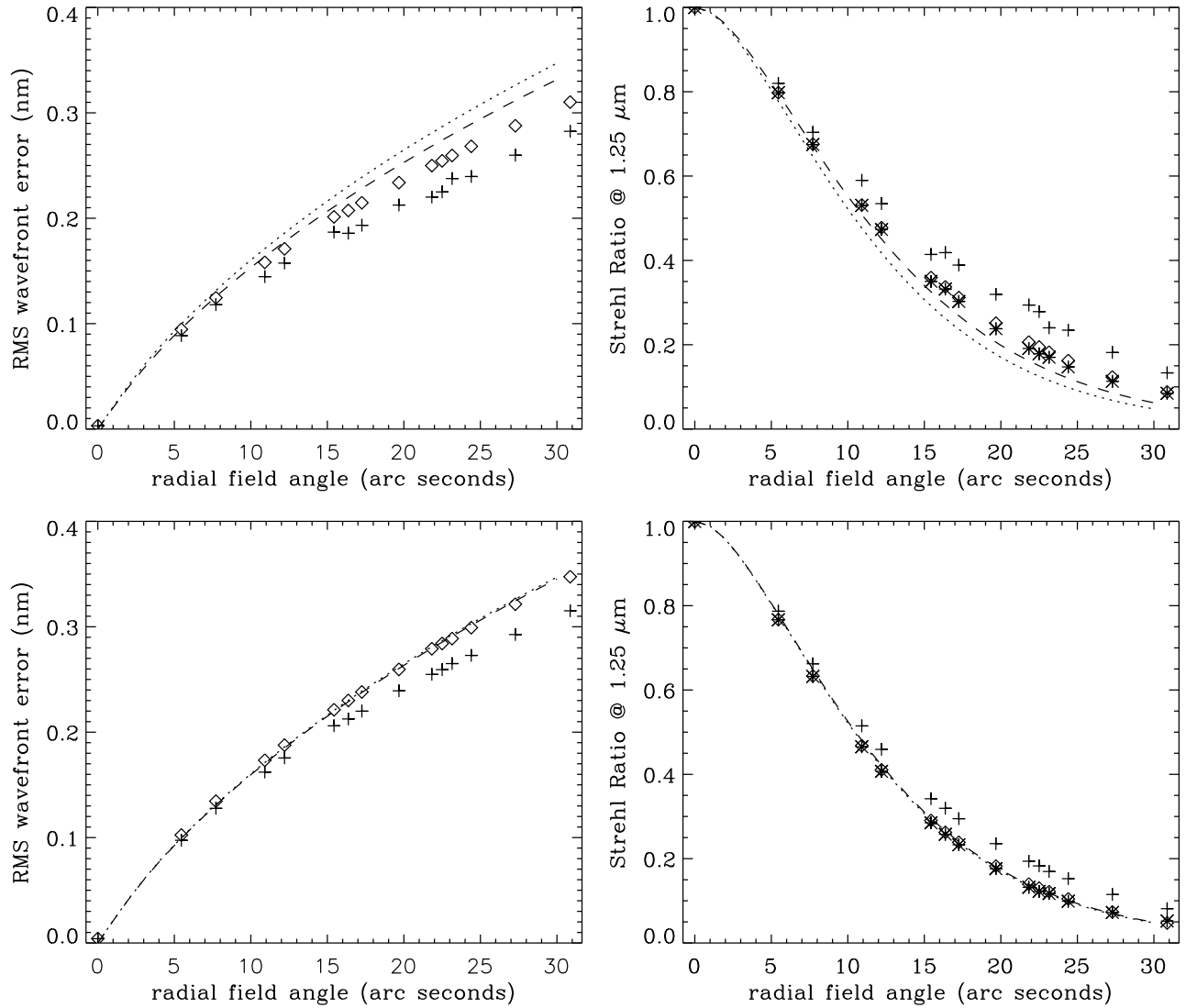


Figure 13: NGS anisoplanatism, comparison between analytical theory and the simulation tool, after 10 (top row) and 50 (bottom row) loop cycles. The theory is shown by the dotted and dashed lines (dotted for the specified input r_0 , dashed for the actual r_0 measured in the loop). The simulation results given are the RMS wavefront error (diamonds) and the tilt-removed error (pluses), as well as the J band Strehl ratio computed both from the PSFs (asterisks) and by the Marechal approximation from the phase variance (diamonds and pluses). After convergence, there is agreement both between the input and actual r_0 , and between the theoretical anisoplanatism curves and the simulation results.